

DEVELOPMENT OF BUBBLE DRIVEN FLOW CFD MODEL APPLIED FOR ALUMINIUM SMELTING CELLS

Y.Q. FENG*, W. YANG, M. COOKSEY and M.P. SCHWARZ

CSIRO Minerals, Clayton, Victoria 3169, AUSTRALIA

* Corresponding author, Yuqing.Feng@csiro.au

ABSTRACT

This paper presents the development of a computational fluid dynamics (CFD) model for the study of bubble driven bath flow in aluminium reduction cells. For validation purpose, the model development was conducted using a full scale air-water model of part of an aluminium reduction cell as a test-bed. The bubble induced turbulence has been modelled by either modifying bubble induced turbulence viscosity directly or by modifying bubble induced turbulence kinetic energy in a standard $k-\varepsilon$ turbulence model. The relative performance of the two modelling approaches has been examined through comparison with experimental data taken under similar conditions using Particle Image Velocimetry (PIV). Detailed comparison has been conducted by point-wise comparison of liquid velocities to quantify the level of agreement between CFD simulation and PIV measurement. Both models can capture the key flow patterns which are comparable with PIV measurement, while the modified turbulence kinetic energy model gives better agreement with flow patterns in the anode cathode distance (ACD).

NOMENCLATURE

C_{up}	bubble induced turbulent eddy viscosity coefficient [-]
C_{TD}	turbulent dispersion force coefficient [-]
C_{CD}	drag force coefficient [-]
C_k	coefficient of bubble induced turbulence kinetic energy [-]
C_ε	coefficient of bubble induced turbulence energy dissipation [-]
$C_{\varepsilon 1}$	turbulence model constants, default values 1.44
$C_{\varepsilon 2}$	turbulence model constants, default values 1.92
d	bubble diameter [m]
k	turbulent kinetic energy [m^2s^{-2}]
M_a	interfacial momentum transfer between phases [$kg\ m^{-1}s^{-2}$]
M^{TD}	Turbulent dispersion force [Nm^{-3}]
P	pressure [Pa]
S_{Ma}	momentum sources due to external body forces [$kg\ m^{-1}\ s^{-2}$]
S_k	bubble induced turbulence kinetic energy [m^2s^{-2}]
S_ε	bubble induced turbulent energy dissipation rate [m^2s^{-3}]
U	velocity [$m\ s^{-1}$]
γ	volume fraction [-]
ε	turbulent energy dissipation rate [m^2s^{-3}]
ρ	density [$kg\ m^{-3}$]
μ	dynamic viscosity [$Pa\cdot s$]

μ_t	turbulent eddy viscosity [$Pa\cdot s$]
μ_{tp}	bubble induced turbulent eddy viscosity [$Pa\cdot s$]
σ	turbulent Prandtl number
σ_k	turbulence model constants, default values 1.0
σ_ε	turbulence model constants, default values 1.3

SUBSCRIPT

c	continuous liquid phase
d	dispersed gas phase
t	turbulence
α	phase, either gas (g) or water (w)

INTRODUCTION

The aluminium reduction cell, or Hall-Heroult cell, is the main unit for primary aluminium production, and involves electrochemical reactions, hydrodynamics driven by anodic gases and electromagnetic forces, and complex heat transfer.

In an aluminium reduction cell, alumina is fed to, and dissolved in, a molten bath of cryolite at approximately 970°C in which the anodes are immersed. Electric current is fed from the anodes to an underlying carbon cathode to cause electrochemical reduction of the alumina to aluminium which settles onto a pool lying over the cathode. CO₂ gas bubbles are generated by the reaction at the anode, and in moving up through the bath under the influence of buoyancy, recirculation flows are set up. Because cryolite will dissolve most potential wall materials, a layer of frozen cryolite must be formed on the walls of the vessel to contain the bath, and this requires a delicate heat balance in the cell, over which the recirculatory flows in the bath have an important influence.

For both economic and environmental reasons, modifications to cell design are being sought to reduce energy and carbon consumption, and to increase productivity (Dias and De Moura, 2005). Multiphase flow and heat transfer are critical to achieving these design improvements.

Detailed investigation of bath flow cannot be made using the aluminium reduction cell itself: the ability to take detailed measurements in real cells is limited because of the high temperature, hostile chemical environment (cryolite) and difficulty of access. Furthermore, the ability to trial unusual operating conditions is constrained by the need to maintain control over the cell operation. Physical and numerical modelling provides the opportunity to determine flows, temperature distributions, current density distributions, etc in great detail, and the ability to trial changes to operating conditions and geometrical configurations without risk. Usually air-water models have been used for model

validation because of ease of operation and also because the two systems possess a similar kinematic viscosity ($8.93 \times 10^{-7} \text{ m}^2 \text{ s}^{-1}$ for water and $1.14 \times 10^{-6} \text{ m}^2 \text{ s}^{-1}$ for cryolite) (Solheim, et al., 1989; Purdie et al., 1993).

A CFD model has been developed to study the effect of key design parameters on bath flow, alumina mixing and equivalent gas layer thickness in ACD for both partial and full cell geometries (Feng et al., 2007a, 2007b, 2010).

For bubble driven flow systems such as aluminium reduction cells, the method of modelling bubble induced turbulence plays an important role in model accuracy. In our early stage of model development (Feng et al., 2006), the bubble induced turbulence was implemented by modifying bubble induced turbulence eddy viscosity. Thereafter, the model has been further developed by modifying bubble induced turbulence kinetic energy.

This paper presents the CFD simulation results obtained by both approaches. The relative performance of the two types of model has been examined through comparison with PIV measurement data conducted under similar conditions. In addition to the general comparison of the overall flow patterns, a point-wise comparison of water velocity has been conducted to quantify the level of agreement between CFD simulation and PIV measurement.

MODEL DESCRIPTION

Governing equations

The governing equations are the continuity and Navier-Stokes equations, essentially conservation equations for mass and momentum.

For the gas-liquid system being studied here, the equations are averaged over the phase structure (i.e. bubbles) so as to give a time-averaged equations for each phase (Schwarz and Turner, 1988; Lane et al., 2005). For this study, they are given as:

Conservation of mass:

$$\nabla \cdot (\gamma_\alpha \rho_\alpha U_\alpha) = 0 \quad (1)$$

Conservation of momentum:

$$\nabla \cdot (\gamma_\alpha (\rho_\alpha U_\alpha \otimes U_\alpha)) = -\gamma_\alpha \nabla P_\alpha + \nabla \cdot (\gamma_\alpha \mu_\alpha (\nabla U_\alpha + (\nabla U_\alpha)^T)) + S_{M\alpha} + M_\alpha \quad (2)$$

where γ_α is the volume fraction of phase α (either gas or water), ρ_α , U_α are the density and vector velocity for phase α , and P and μ are the pressure and effective viscosity. $S_{M\alpha}$ describes momentum sources due to external body forces, e.g. buoyancy and electromagnetic force (the electromagnetic force is not included in the water flow model). M_α describes the interfacial momentum transfer between phases and can include several types, such as the drag force, lift force, virtual mass, wall lubrication force, inter-phase turbulent dispersion force, etc. The effective viscosity is the sum of molecular (dynamic) viscosity (μ_0) and turbulent viscosity (μ_t).

Phase dependent turbulence models have been used: the dispersed phase zero equation model for gas phase and the k - ε two-equation model for the liquid phase. The turbulence eddy viscosity is calculated as:

$$\mu_{td} = \frac{\rho_d \mu_{tc}}{\rho_c \sigma} \quad (3)$$

for the gas phase and :

$$\mu_{tc} = c_\mu \rho_c \frac{k_c^2}{\varepsilon_c} \quad (4)$$

for the liquid phase.

The subscript c denotes the continuous liquid phase and d denotes the dispersed gas phase. The parameter σ is a turbulent Prandtl number relating the dispersed phase kinematic eddy viscosity to the continuous phase kinematic eddy viscosity. c_μ is the k - ε turbulent model constant (default value 0.09), and k and ε are turbulence kinetic energy and turbulence dissipation rate respectively. As is standard practice, the transport equations for k and ε are assumed to take a form similar to the single-phase transport equations:

$$\nabla \cdot (\gamma_\alpha (\rho_\alpha U_\alpha k_\alpha)) - (\mu + \frac{\mu_{td}}{\sigma_k}) \nabla k_\alpha = \gamma_\alpha (P_\alpha - \rho_\alpha \varepsilon_\alpha) + S_k \quad (5)$$

$$\nabla \cdot (\gamma_\alpha (\rho_\alpha U_\alpha \varepsilon_\alpha)) - (\mu + \frac{\mu_{td}}{\sigma_\varepsilon}) \nabla \varepsilon_\alpha = \gamma_\alpha \frac{\varepsilon_\alpha}{k_\alpha} (C_{\varepsilon 1} P_\alpha - C_{\varepsilon 2} \rho_\alpha \varepsilon_\alpha) + S_\varepsilon \quad (6)$$

where $C_{\varepsilon 1}$, $C_{\varepsilon 2}$, σ_k , σ_ε are turbulence model constants, default values being 1.44, 1.92, 1.0 and 1.3 respectively. P_α is the turbulence production due to viscous production. S_k and S_ε represent inter-phase transfer for k and ε respectively.

Solving equations (1-6) cannot achieve an accurate solution to represent the complex multiphase systems. Extra model input is required to represent the real physics, of which, two important factors are bubble induced turbulence and bubble induced turbulent dispersion force.

Bubble induced turbulence

Bubbles rising in the molten bath will give rise to increased turbulence of the liquid phase, known as bubble-induced turbulence. Various models have been proposed in the literature to account for this mechanism, with the two most widely accepted being modifying bubble induced turbulence eddy viscosity (Sato and Sekoguchi, 1975) and adding a source of bubble induced turbulent kinetic energy. Bubble induced turbulence is very case dependent, which prevents a universal form for general use and is still an active area of research, as reviewed by Sokolichin et al. (2004). For this study, the commonly used form for vertical pipe bubbling flow is used and is given as follows.

For the model with modified bubble induced turbulence eddy viscosity, an additional term of the following form is added to the effective viscosity:

$$\mu_{tp} = C_{\mu p} \rho_c (1 - \gamma_c) d_p (U_c - U_d) \quad (7)$$

where $C_{\mu p}$ is the bubble induced turbulent eddy viscosity coefficient.

For the model with a modified turbulence kinetic energy equation, a source term in the following forms has been added to the k - ε equations:

$$S_k = C_k \rho_c (1 - \gamma_c) (U_c - U_d)^2 \quad (8)$$

$$S_\varepsilon = \frac{C_\varepsilon}{C_k} \frac{\varepsilon}{k} S_k \quad (9)$$

where C_k and C_ε are the coefficients of bubble induced turbulence kinetic energy and energy dissipation respectively.

Bubble induced turbulence dispersion force

A turbulence dispersion force is proposed in the literature to account for the diffusion of bubbles due to the random influence of turbulent eddies in the liquid. The Favre averaged turbulence dispersion force model, an option in the ANSYS CFX12 Solver, has been used in this study.

The form is given as:

$$M_c^{TD} = -M_d^{TD} = -C_{TD} C_{cd} \frac{U_{ic}}{\sigma_{ic}} \left(\frac{\nabla \gamma_d}{\gamma_d} - \frac{\nabla \gamma_c}{\gamma_c} \right) \quad (10)$$

Universally applicable values for the coefficient listed in equations 7-10 cannot be obtained from the literature (Moraga et al., 2003). In this project, physical measurements are used to help determine an appropriate value on a trial-and-error basis. Considering bubble induced turbulence is suppressed beneath anodes, the value in this region is set to a small value. Table 1 lists the values used for this study.

Table 1: Coefficients for bubble induced turbulence

	C_{TP}	C_k	C_ε	C_{TD}
ACD	1	1	1	0.025
Other region	20	20	20	0.2

Modelling conditions

For model validation purposes, the CFD modelling setup was based on a three anode air-water model. A diagram of the physical model (constructed of Perspex) is shown in Figure 1.

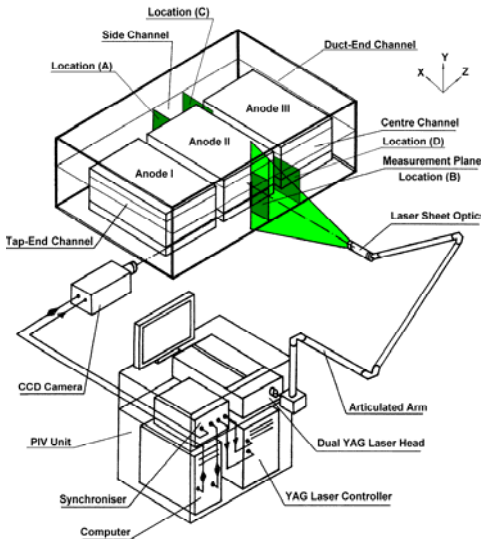


Figure 1: Three-anode physical model, showing arrangement of PIV measurement for vertical planes.

The detailed configuration can be found in a previous publication (Cooksey and Yang, 2006). A few key

parameters are described here for convenience of discussion.

The anode dimensions (1300 mm x 650 mm x 600 mm) were selected to be the same as those typical of a modern pre-bake smelter (not a specific anode design). Other parameters were set as follows:

ACD:	40 mm
Anode slope:	0°
Tap-end channel:	160 mm
Duct-end channel:	40 mm
Side channel:	240 mm
Centre channel:	120 mm
Liquid depth:	200 mm
Gas flow rate for each anode:	120 L min ⁻¹

PIV measurement was conducted over five planes: four vertical planes (Locations (A) to (D) in Figure 1) and a horizontal plane in the middle of the ACD. It is believed that these five planes can describe the key flow structures in the 3D model and provide sufficient data for CFD model validation.

A commercial CFD code (ANSYS-CFX12) has been used to obtain a solution of these equations. The boundary conditions are set as following:

- a gas inlet to the computational domain on the bottom surface of the anode representing gas generation by reduction;
- a gas outlet on the top surface of the liquid pool at which gas leaves the bath at the rate it arrives from below (i.e. a so-called “degassing condition”);
- the other solid boundaries were set as walls (no slip for water and free slip for air).

On the basis of observation of the water model, bubble size was taken to be uniform size with 0.01 m in diameter. Due to the lack of information concerning drag forces for bubbles moving under a horizontal surface, as stated in previous publication (Solheim et al., 1989), the same drag force correlation has been applied to the whole cell. Momentum exchange through drag force is calculated according to Ishii and Zuber (1979) correlations, which are readily available in the CFX solver.

RESULTS AND DISCUSSION

CFD vs PIV: overall flow patterns

Velocity vectors and streamlines are plotted for a visual comparison between PIV measurement and CFD simulation. Figures 2 to 5 show the water flow over the four vertical planes. One common feature of the flow in these planes is the presence of a local recirculation zone. At the mid-point of Anode II (Figures 2 and 3), bubbles released from the anode bottom change direction and rise upward at the anode edge due to the buoyancy force. Consequently, water is pumped upward, and flows almost vertically. The water flow changes its direction horizontally toward the outer wall at the liquid surface, followed by a vertically downward flow close to the outer wall, completing the recirculation by joining the upward flow. These flow patterns have been predicted by

CFD simulations either by modifying bubble induced turbulence eddy viscosity (Figure 2b and Figure 3b) or modifying bubble induced turbulence kinetic energy (Figure 2c and Figure 3c).

At the mid-point of the inter-anode gap (Figures 4 and 5), the recirculation zone is formed by bubbles released into the inter-anode gap which pump water towards both the side channel (Figure 4) and the centre channel (Figure 5).

Figure 6 shows the bath flow in a horizontal plane at the mid-point of ACD. It is interesting to see that such a complex flow (Figure 6a) has been successfully predicted by both types of models. The model prediction by modifying bubble induced turbulence kinetic energy (Figure 6c) is in closer agreement than the prediction by modifying bubble induced turbulence eddy viscosity

(Figure 6b) in terms of streamline pattern and velocity magnitude. The water flow velocity is much stronger in the side and centre channels than beneath the anode. Water flows towards the ACD from the wider end channel (tap end) and flows out from the ACD at the narrower end channel (duct end). In the ACD under Anode II, water travels further from the wider side channel before diverging to the inter-anode gap than from the narrower centre channel. These observations demonstrate a significant effect of channel width on flow structures. For example, when the channel is narrow as at the duct end, the water pumped up by bubbles can not form local recirculations, and mainly flows out towards the side and centre channels. Water in the ACD has to flow in to replace the water pumped out from the ACD.

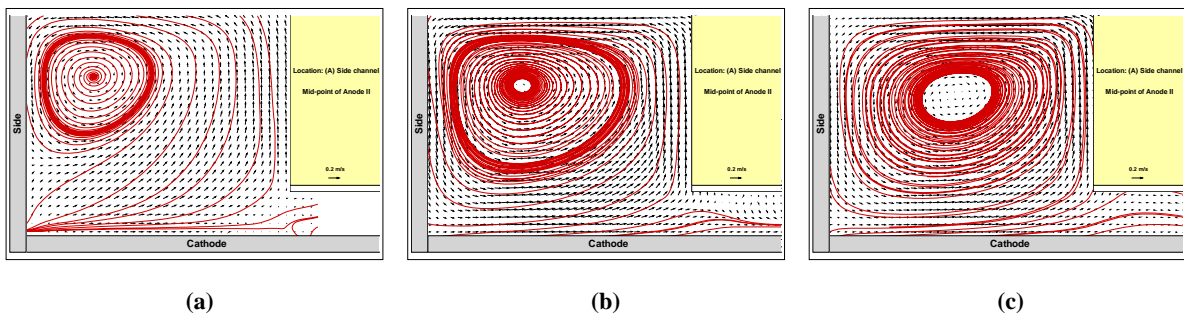


Figure 2: Water velocity distribution and streamlines at location (A) in figure 1: (a) PIV measurement; (b) CFD simulation by modifying turbulent eddy viscosity; (c) CFD simulation by modifying turbulence kinetic energy.

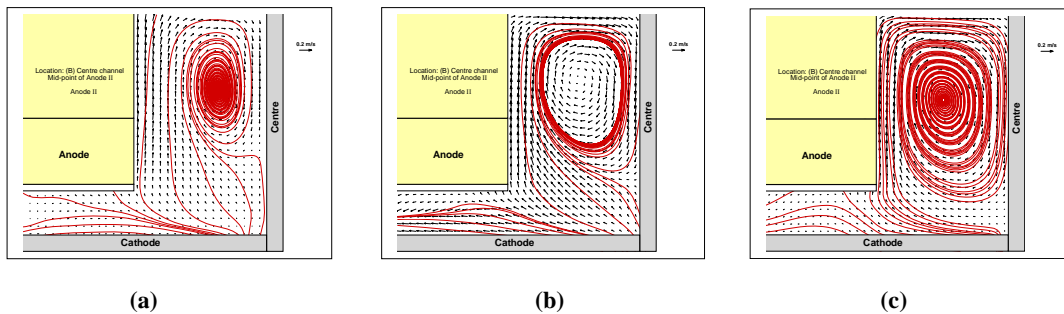


Figure 3: Water velocity distribution and streamlines at location (B) in figure 1: (a) PIV measurement; (b) CFD simulation by modifying turbulent eddy viscosity; (c) CFD simulation by modifying turbulence kinetic energy.

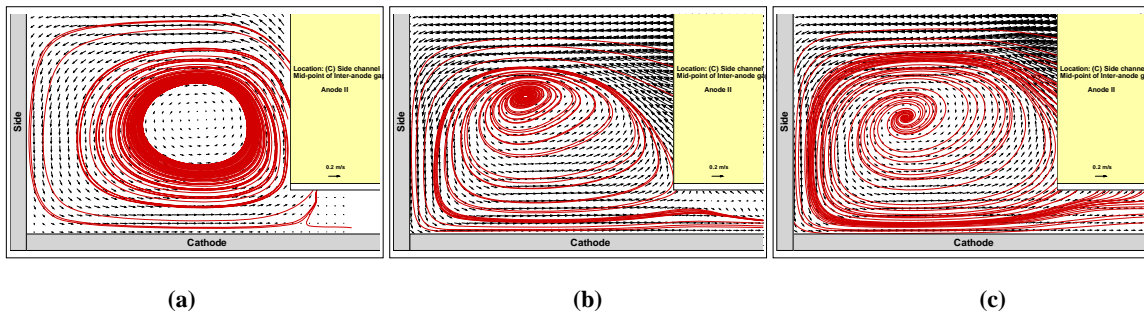


Figure 4: Water velocity distribution and streamlines at location (C) in figure 1: (a) PIV measurement; (b) CFD simulation by modifying turbulent eddy viscosity; (c) CFD simulation by modifying turbulence kinetic energy.

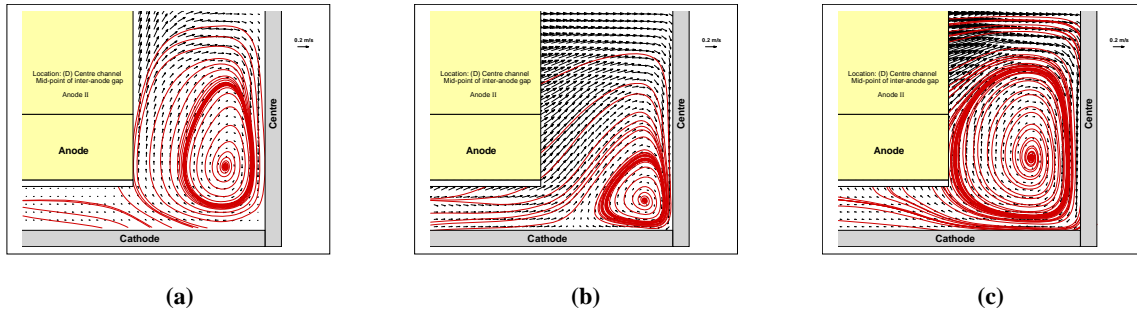


Figure 5: Water velocity distribution and streamlines at location (D) in figure 1: (a) PIV measurement; (b) CFD simulation by modifying turbulent eddy viscosity; (c) CFD simulation by modifying turbulence kinetic energy.

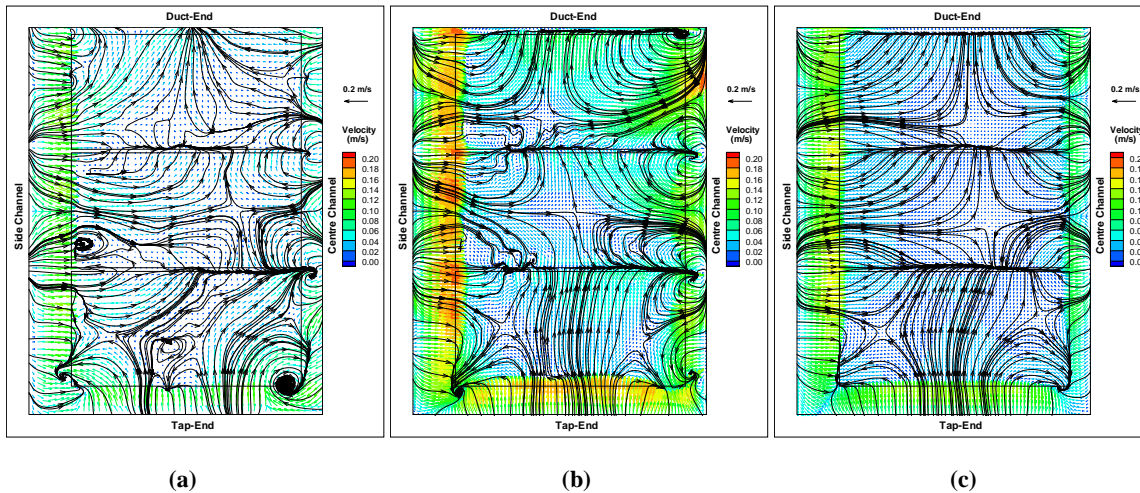


Figure 6: Water velocity distribution and streamlines at a horizontal plane in middle of ACD: (a) PIV measurement; (b) CFD simulation by modifying turbulent eddy viscosity; (c) CFD simulation by modifying turbulence kinetic energy.

PIV vs CFD: a detailed comparison

The complexity of the bath flow may constrain an exact point-wise match between CFD simulation and PIV measurement. However, it is useful to perform a detailed comparison to quantify the level of agreement.

A quantitative comparison of the horizontal and vertical velocity component was conducted on a line-by-line basis at three heights in the measured four vertical planes (Figures 7 to 10). The vertical positions selected for comparison are 0.08, 0.12 and 0.16 m from the water bottom, which represents $\frac{1}{4}$, $\frac{1}{2}$ and $\frac{3}{4}$ of the anode height. For the vertical component of velocity, a positive value represents an upward motion. For the horizontal component, a positive value signifies the flow direction from the centre channel towards the side channel. The x-axis in Figures 7 to 10 shows the horizontal location with the outside wall of the centre channel setting zero, representing the centre of the centre channel in an industrial cell.

Generally, the two types of method for modifying bubble induced turbulence predict similar level of agreement. For most of the locations, the agreement between PIV measurement and CFD prediction is good. The biggest difference is at higher positions in the inter-anode gap at both the side channel (Figure 9) and centre channel (Figure 10), where the simulated horizontal velocities are much higher than PIV measurement. This difference is consistent with the flow visualization shown in Figures 4 and 5: the CFD simulations show that water flows almost

horizontally out from the inter-anode gap towards both the side and centre channels, while the PIV measurements show a strong upward motion. A bias in the PIV measurements in the bubbly region might be one reason for this difference, as the flow in the bubble region cannot be accurately measured by PIV. On the other hand, the model setup with uniform bubble size may not fully represent the bubble behaviour in the inter-anode gap. The cause for this large difference will be investigated further in the future.

CONCLUSIONS

Using a full scale air-water model of part of an aluminium reduction cell as a test-bed, a time-averaged bubble driven flow model has been developed. The bubble induced turbulence has been modelled either by modifying bubble induced turbulence viscosity or bubble induced turbulence kinetic energy in a standard $k-\epsilon$ turbulence model. The relative performance of the two types of modelling approach has been examined through comparison with experimental data taken under similar conditions using PIV measurement. Both models can predict key flow patterns which are comparable with PIV measurement, while the modified turbulence kinetic energy model gives better agreement in flow patterns in ACD in terms of both flow patterns and the velocity magnitude. Detailed comparison has been conducted by point-wise comparison of liquid velocity in the side and centre channels, which show good agreement for most locations.

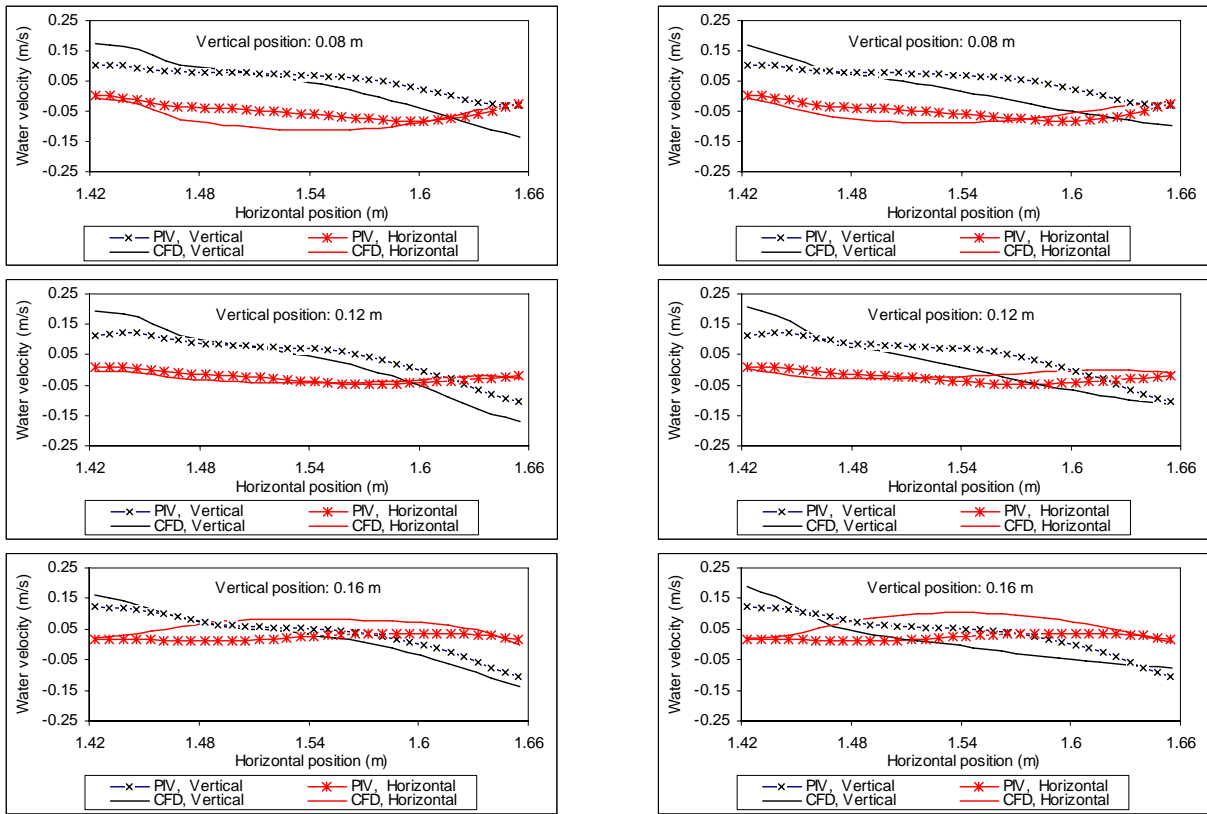


Figure 7: Point-wise comparison of water velocity between PIV measurement and CFD simulation at location (A) in figure 1: Left, CFD simulation by modifying turbulent eddy viscosity; Right, CFD simulation by modifying turbulence kinetic energy.

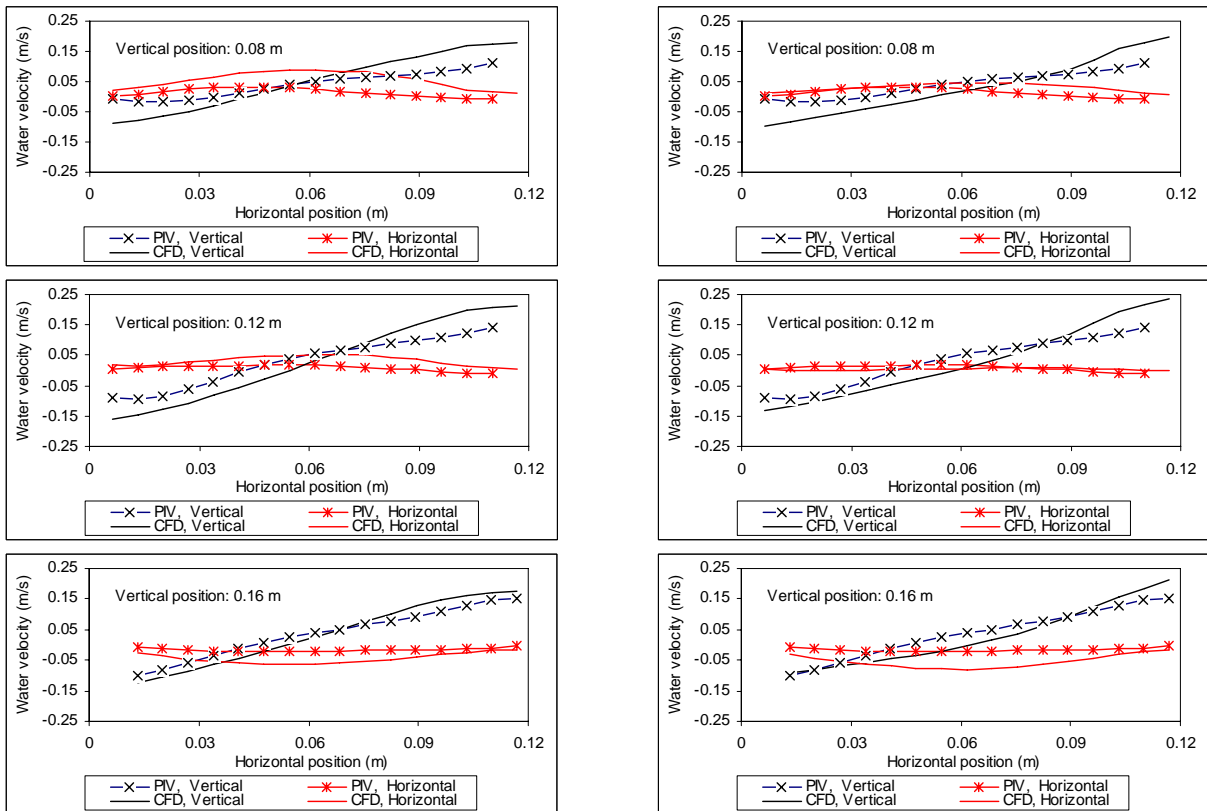


Figure 8: Point-wise comparison of water velocity between PIV measurement and CFD simulation at location (B) in figure 1: Left, CFD simulation by modifying turbulent eddy viscosity; Right, CFD simulation by modifying turbulence kinetic energy.

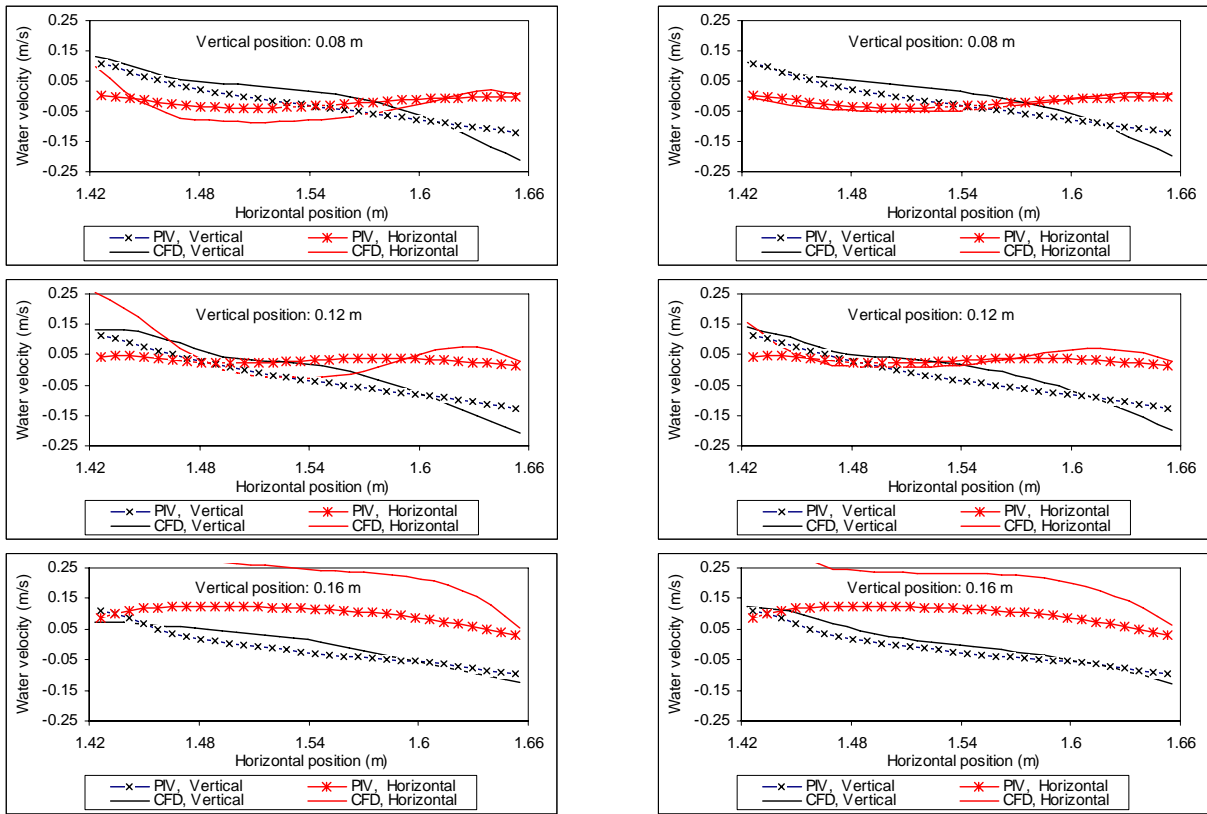


Figure 9: Point-wise comparison of water velocity between PIV measurement and CFD simulation at location (C) in figure 1: Left, CFD simulation by modifying turbulent eddy viscosity; Right, CFD simulation by modifying turbulence kinetic energy.

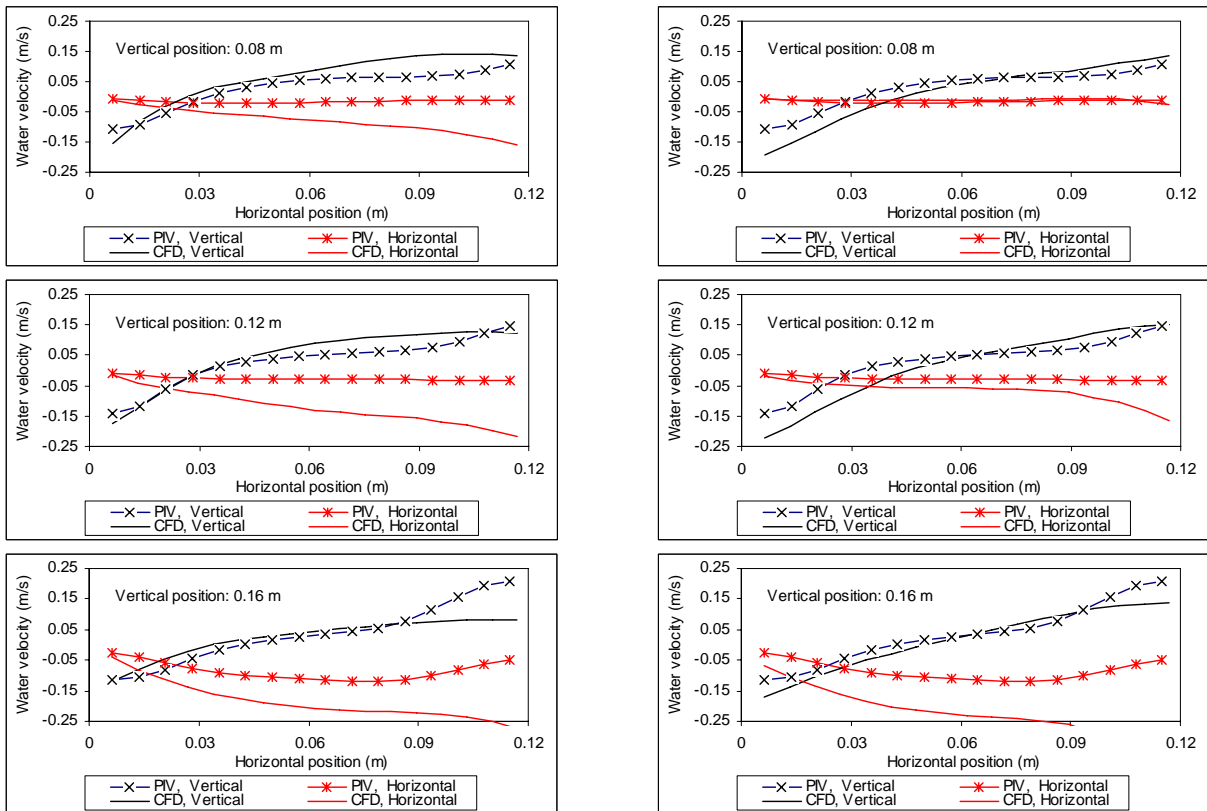


Figure 10: Point-wise comparison of water velocity between PIV measurement and CFD simulation at location (D) in figure 1: Left, CFD simulation by modifying turbulent eddy viscosity; Right, CFD simulation by modifying turbulence kinetic energy.

ACKNOWLEDGEMENTS

The work was conducted under the auspices of the CSIRO Light Metals Flagship.

REFERENCES

- ANSYS CFX 12 User manual, ANSYS Inc.
- COOKSEY, M.A. and YANG, W., (2006), "PIV measurements on physical models of aluminium reduction cells", *Light Metals*, 359-365.
- FENG, Y.Q., YANG, W., COOKSEY, M.A. and SCHWARZ, P., "CFD model of bubble driven flow in aluminium reduction cells and validation using PIV measurement", 5th International Conference on Computational Fluid Dynamics in the Process Industries, Melbourne, Australia, 2006.
- FENG, Y.Q., COOKSEY, M.A. and SCHWARZ, P., "CFD modelling of electrolyte flow in aluminium reduction cells", *Light Metals 2007*, Orlando, FL, 2007a, 339-344.
- FENG, Y.Q., COOKSEY, M.A. and SCHWARZ, P., "Development of Whole Cell Model of Bath Flow and Alumina Mixing", 9th Australasian Aluminium Smelting Technology Conference, 2007b, 14pp.
- FENG, Y.Q., COOKSEY, M.A. and SCHWARZ, P., "CFD modelling of alumina mixing in aluminium reduction cells", accepted by TMS 2010.
- DIAS, H.P. and DE MOURA, R.R., (2005), "The use of transversal slot anodes at Albras smelter", *Light Metals*, 341-344.
- ISHII, M. and ZUBER, N., (1979), "Drag coefficient and relative velocity in bubbly, droplet or particulate flows", *AIChE J.*, **25**, 843-855.
- LANE, G. L., SCHWARZ, M. P., and EVANS, G. M., (2005). "Numerical modelling of gas-liquid flow in stirred tanks", *Chemical Engineering Science*, 60, 2203-2214.
- MORAGA, J.F., LARRELEGUY, A.E., DREW, D.A. and LAHEY, R.T., (2003), "Assessment of turbulent dispersion models for bubbly flows in the low stokes number limit", *Int. J. Multiphase Flow*, 29, 655-673.
- PURDIE, J.M., Bilek, M., Taylor, M.P., Zhang, W.D., Welch, B.J. and Chen, J.J.J., "Impact of anode gas evolution on electrolyte flow and mixing in aluminium electro-winning cells", *Light Metals*, 1993, 355-360.
- SATO, Y. and SEKOGUCHI, K., (1975), "Liquid velocity distribution in two-phase bubbly flow", *Int. J. Multiphase Flow*, 2, 79.
- SCHWARZ, M.P. and TURNER, W.J., (1988), "Applicability of the standard k- ϵ turbulence model to gas-stirred baths", *Appl. Math. Modelling*, 12, 273-279.
- SOKOLICHIN, A., EIGENBERGER, G. and LAPIN, A., (2004), "Simulation of buoyancy driven bubbly flow: established simplifications and open questions", *AIChE Journal*, 50, 24-44.
- SOLHEIM, A., JOHANSEN, S.T., ROLSETH, S. and THONSTAD, J., (1989), "Gas induced bath circulation in aluminium reduction cells", *Journal of Applied Electrochemistry*, 19, 703-712.